arXiv:2507.17883v1 [cond-mat.soft] 23 Jul 2025

Differential Crosslinking and Contractile Motors Drive Nuclear Chromatin Compaction

Ligesh Theeyancheri,[1,*] Edward J. Banigan,[2,†] and J. M. Schwarz[1,3,‡]

[1] *Physics Department, Syracuse University, Syracuse, NY 13244 USA*
[2] *Institute of Medical Engineering & Science and Department of Physics, Massachusetts Institute of Technology, Cambridge, MA 02139, USA*
[3] *Indian Creek Farm, Ithaca, NY 14850 USA*

During interphase, a typical cell nucleus features spatial compartmentalization of transcriptionally active euchromatin and repressed heterochromatin domains. In conventional nuclear organization, euchromatin predominantly occupies the nuclear interior, while heterochromatin, which is approximately 50% more dense than euchromatin, is positioned near the nuclear periphery. Peripheral chromatin organization can be further modulated by the nuclear lamina, which is itself a deformable structure. While a number of biophysical mechanisms for compartmentalization within rigid nuclei have been explored, we study a chromatin model consisting of an active, crosslinked polymer tethered to a deformable, polymeric lamina shell. Contractile motors, the deformability of the shell, and the spatial distribution of crosslinks all play pivotal roles in this compartmentalization. We find that a radial crosslink density distribution, even with a small linear differential of higher crosslinking density at the edge of the nucleus, combined with contractile motor activity, drives genomic segregation, in agreement with experimental observations. This arises from contractile motors preferentially drawing crosslinks into their vicinity at the nuclear periphery, forming high-density domains that promote heterochromatin formation. We also find an increased stiffness of nuclear wrinkles given the preferential heterochromatin compaction below the lamina shell, which is consistent with instantaneous nuclear stiffening under applied nanoindentation. We conclude with the potential for experimental validation of our model predictions.

I. INTRODUCTION

The cell nucleus plays a vital role in eukaryotic cells by enclosing and safeguarding genetic information encoded within chromatin polymer fibers composed of DNA and histone proteins [1, 2]. Collectively, these polymer fibers constitute spatially partitioned chromatin states within the nucleus, broadly known as euchromatin and heterochromatin. Euchromatin is the gene-rich, transcriptionally active, and loosely packed form, while heterochromatin is gene-poor, transcriptionally inactive, and densely packed [3, 4]. In conventional nuclear organization, euchromatin resides in the nuclear interior, while heterochromatin is localized at the nuclear periphery [3–5], with a density difference of 50% or more between the two [6, 7].

Recent studies suggest several plausible explanations for spatial segregation of peripheral heterochromatin and interior euchromatin concentrated in the inner nuclear region. There is substantial evidence that compartmentalization of the genome can result from mesoscale phase separation [8–21], with peripheral heterochromatin maintained by attractive interactions with the lamina [15, 19, 22, 23]. Besides affinity-mediated interactions, differences in the other physical properties of heterochromatin and euchromatin may also contribute to their partitioning. Nuclear elastography measurements indicate that heterochromatin may be almost four times stiffer than euchromatin [24]; simulations predict that the conventional nuclear chromatin organization can be obtained by increasing the bending stiffness of the heterochromatin relative to euchromatin [25–27]. Entropic effects from nonspecific protein binding may further contribute to chromatin compaction, clustering, and compartmentalization [28, 29]. In addition to equilibrium effects, a number of studies suggest that compartmentalization of the genome can result from *nonequilibrium* mesoscale phase separation driven by heterogeneous activity [30–39].

While a nonequilibrium phase separation approach may provide a basis for chromatin compartmentalization, as the cell nucleus is an out-of-equilibrium system, chromatin and the nucleus also exhibit highly nontrivial dynamics. Specifically, various experiments observe micron-scale correlated movement of genomic regions over seconds [40–46]. This correlated motion is reduced in the absence of ATP or by reduction of activity by motors, such as transcribing RNA polymerases [40, 41, 44, 47]. At the same time, the deformable lamina shell exhibits a broadly distributed power spectrum [48]. It has been demonstrated that both the correlated chromatin motion and the power spectrum can be quantitatively understood with an active, crosslinked polymeric system confined within a deformable shell [49]. These correlated motions are thought to drive dynamic nuclear shape deformations, such as wrinkles, bulges, and "blebs", chromatin-filled

* ligeshbhaskar@gmail.com
† ebanigan@mit.edu
‡ jmschw02@syr.edu

nuclear protrusions that are prone to rupture [50, 51]. Given these findings, we ask to what extent the dynamic architecture of the cell nucleus may be explained by the physics of active polymers. Specifically, is motor activity combined with connectivity within chromatin sufficient to compartmentalize chromatin into different forms, particularly euchromatin and heterochromatin?

Here, we report progress towards answering this question to arrive at a simple, novel biophysical mechanism for chromatin compartmentalization based on motor activity and varying spatial profiles of chromatin crosslinking. Various molecular motors and enzymes operate throughout chromatin, including RNA polymerase II and cohesin [52, 53]. Likewise, various DNA- and chromatin-binding proteins may act as crosslinkers by bridging chromatin sites. In particular, heterochromatin protein 1 (HP1) is a crucial mediator of chromatin crosslinking and can be found in both heterochromatin and euchromatin [54–59]. HP1's diverse roles, including heterochromatin formation, gene silencing, telomere maintenance, DNA replication, and repair, suggest that the interactions of HP1 with neighboring protein complexes may play a significant role in regulating its ability to crosslink chromatin. Therefore, the localization of other protein complexes, such as Cullin 4B (CUL4B), interacting with HP1 could lead to a spatial distribution of crosslinks within the nucleus [60].

With this biological context, our model incorporates simple extensile and contractile monopolar motor activities, representative of ATP-driven processes in the nucleus [47, 49, 50, 61]. We also implement chromatin crosslinks that mimic chromatin-binding proteins like HP1 [54, 56, 57, 62]. To capture the effects of differential HP1 localization in the nucleus, we vary the spatial distribution of crosslinks using uniform, linear, and inverted radial crosslink profiles. Additionally, our model accounts for the deformable nature of the nuclear envelope, as the lamina is soft and undergoes shape fluctuations [48, 49, 63, 64]. We hypothesize that patterning of physical constraints within chromatin that regulate chromatin spatial organization and facilitate mechanoresponses and dynamic adaptation of the nucleus and genome to internal and external perturbations [2, 57, 64–71].

II. MODEL

The chromatin-lamina system is modeled with the chromatin represented as a Rouse chain and the lamina as an elastic, polymeric shell, with linkages between the chain and the shell [49, 72, 73]. More specifically, monomers in the lamina shell are connected by Hookean springs with spring constant K. In the initial preparation of the shell, a Fibonacci sphere with 5000 nodes is generated and 5000 identical monomers are placed at these nodes. The monomers connected by springs form a mesh with an average coordination number of 4.5. The monomers have soft-core repulsive interactions to model excluded volume. The chromatin fiber, on the other hand, is modeled by a Rouse chain with soft-core repulsion between each monomer, which has radius $r_p = 0.43089$. A three-dimensional self-avoiding random walk in an FCC lattice is performed to generate the polymer with $N = 5000$ monomers. Subsequently, the chromatin polymer is packed in a hard spherical shell before equilibration. The monomers of the shell have the same physical properties as the chain monomers in terms of size (r_s) and spring constant.

Initial configurations of the lamina and the chromatin confined within are generated using the following protocol [49]. The spherical shell is gradually shrunk by moving its monomers inward, which in turn drives the chain monomers inward due to soft-core repulsions. Once the target radius is reached, the positions of the shell monomers are relaxed, and the spring lengths are updated to finalize the initial system configuration (Fig. S1). With the initial shell radius, $\mathrm{R}_s = 10$, the resulting volume fraction is $\phi_{pack} \approx 0.4$ prior to further relaxation. We repeat this process and generate 50 initial configurations. We define the simulation units such that one unit of length corresponds to 1 μm, one unit of time is 0.5 seconds, and the energy scale is $k_BT = 10^{-21}$ J, where $T = 300$ K (a complete list of simulation parameters is provided (Table S1) in the supporting information (SI)).

We implement the excluded volume interactions using a repulsive, soft-core potential between any two monomers, i and j, which are separated by a distance $|\vec{r}_{ij}|$, modeled using:

$$V_{\mathrm{Ex}}(r_{ij}) = \begin{cases} \frac{1}{2}K_{\mathrm{Ex}}\left(|r_{ij}| - \sigma_{ij}\right)^2 & \text{if } |r_{ij}| < \sigma_{ij}, \\ 0 & \text{otherwise,} \end{cases} \quad (1)$$

where $\sigma_{ij} = r_{p_i} + r_{p_j}$. We also incorporate crosslinks in chromatin [57], tethering of chromatin to the lamina, and motor activity within the chromatin polymer (Fig. 1). We establish a total of N_c crosslinks in the chromatin by adding springs between randomly selected pairs of polymer monomers, where the springs have the same stiffness, K, as those connecting adjacent monomers along the polymer chain. A crosslink may be established if the distance between the selected monomers is less than $r_{\mathrm{link}} = 3r_p$.

To investigate how the distribution of crosslinks influences the spatial organization of chromatin within the nucleus, we consider three distinct (initial) crosslinking profiles: uniform, linear, and inverted (Fig. 1d). In the uniform profile, crosslinks are formed randomly between any N_c pairs of monomers. The linear profile involves a linearly increasing crosslink density from the center of

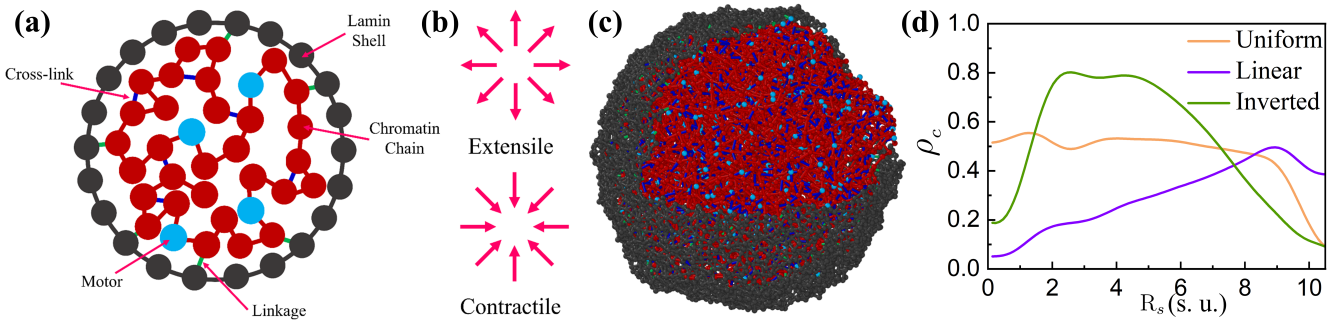


Fig. 1: *3D computational model of chromatin in a deformable nucleus.* (a) A two-dimensional schematic of the model. (b) A schematic illustrating the two types of motors acting on the chromatin. (c) A Simulation snapshot. The chromatin polymer consists of linearly connected monomers, depicted in red, while the active chromatin subunits are shown in cyan. The lamina is made up of lamin subunits, represented in grey. (d) The radial distribution of crosslink density (ρ_c) as a function of nuclear radius R_s. All quantities are reported in simulation units (s. u.), where 1 s. u. of length = 1 μm.

the nucleus toward the nuclear periphery. Conversely, in the inverted profile, the crosslink density increases linearly from the nuclear periphery toward the center of the nucleus. Crosslinks are assigned at the start of the simulation by dividing the nucleus into concentric spherical shells of equal volume and assigning a radial probability distribution for crosslink formation across these shells. For the i^{th} shell, the probability of forming a crosslink is proportional to $\frac{r_i}{R_s}$ for the linear profile or $1 - \frac{r_i}{R_s}$ for the inverted profile, where r_i is the shell center and R_s is the nuclear center. This implies that the probability at the exact center is minimal due to the finite width of the innermost shell. Crosslinks are initialized once at the start of the simulation and remain topologically fixed throughout, although their spatial configuration evolves dynamically. The slope of the radial crosslinking profile remains fixed across simulations with different total numbers of crosslinks. This framework allows us to analyze how different spatial distributions and concentrations of crosslinks affect the three-dimensional arrangement of chromatin inside the nucleus.

A total of N_L random polymer-shell linkages are introduced to model connections between chromatin and the nuclear lamina [70, 74, 75]. In addition to thermal fluctuations, we incorporate motor activity by designating N_m chromatin monomers as active [49, 50]. An active monomer exerts a force $\boldsymbol{F_a} = \pm f_m \hat{r}_{ij}$ on other monomers within a specified range. f_m denotes the strength of the motor force. The motors can exert either extensile or contractile forces, pushing the monomers apart or drawing them together (Fig. 1b), analogous to other models that explicitly account for motor activity [47, 61]. A motor stochastically unbinds from a monomer with characteristic turnover time, $\tau_m = 20$, after which the monomer becomes passive and the motor binds to another randomly selected chromatin monomer, which will then exert active forces. The timescale $\tau_m \approx 10$ s is comparable to the timescale of experimentally observed chromatin motions [40, 41].

The system evolves through Brownian dynamics, governed by the overdamped equations of motion:

$$\xi \dot{\boldsymbol{r}}_{\boldsymbol{i}} = \boldsymbol{F_{Ex}} + \boldsymbol{F_{Sp}} + \boldsymbol{F_{Th}} + \boldsymbol{F_{Ac}} + \boldsymbol{f_n}(t), \qquad (2)$$

where $\boldsymbol{r_i}$ represents the position of the i^{th} monomer at time t, and ξ is the friction coefficient, which is related to the thermal Gaussian noise, $\boldsymbol{f_n}(t)$, via the fluctuation-dissipation theorem. $\boldsymbol{F_{Ex}}$ represents the force arising from excluded volume interactions, $\boldsymbol{F_{Sp}}$ accounts for the harmonic forces generated by polymer chain springs, chromatin crosslink springs, and chromatin-lamina linkage springs, and $\boldsymbol{F_{Th}}$ corresponds to the thermal forces, and $\boldsymbol{F_{Ac}}$ denotes the force due to the contractile or extensile motors. For the passive system, no motors are present, and the active force $\boldsymbol{F_{Ac}}$ is set to zero. We employ the Euler method for time integration, with a time step of $d\tau = 10^{-4}$, and a total simulation time of $\tau = 10^3$. To evaluate the structural properties in the steady state, we measure the radius of gyration, R_g, and average radius of the lamina shell, $\langle R_s \rangle$. The system is considered to be in steady state when these quantities no longer exhibit significant changes over time (Fig. S2).

III. RESULTS

As we consider different types of motors and different crosslinking profiles, we also use a reference configuration, the chromatin distribution in the absence of both crosslinks and chromatin–lamina linkages, as well as in systems with lamina linkages but no crosslinks (Fig. S3). Without chromatin-lamina linkages, chromatin accumulates at the center of the simulated nucleus, particularly in the scenario with contractile motors. This result suggests that chromatin-lamina linkages are essential to prevent excess accumulation of chromatin in the interior.

In the following subsections, we systematically analyze how these molecular motors and crosslinks can establish conventional heterochromatin-euchromatin organization inside the nucleus.

A. Radial chromatin distribution governed by motor activity and crosslink profile

To quantify the effect of the crosslink distribution on the radial chromatin density, ϕ_c, we compute ϕ_c by dividing the nuclear volume into concentric shells of equal width, counting the number of chromatin monomers in each shell, and normalizing by shell volume. Fig. 2 depicts ϕ_c *vs.* radial position, R_s, for both initial configurations and steady states across passive, extensile, and contractile motor conditions with varying crosslink profiles. The initial chromatin distribution in the nucleus is uniform regardless of the crosslink density profile, as shown in Fig. 2a. As the system evolves, chromatin spatial organization changes in response to the interplay of crosslinks and motor activity.

To distinguish the contribution of motor activity, we first examine the passive case without motors, where density profiles depend on the crosslink distribution. The uniform and linear crosslink profiles yield homogeneously distributed chromatin across R_s, while the inverted crosslink profile generates higher chromatin density in the nuclear interior (Fig. 2b).

Motor activity alters the spatial pattern of chromatin density, depending on the crosslink distribution. Upon introducing extensile motors, chromatin localizes more toward the center in simulations with uniform and inverted crosslink density profiles. In contrast, with linear crosslink profiles, we observe a nearly uniform chromatin distribution as a function of R_s, with slightly elevated chromatin concentration at the periphery (Fig. 2c). Notably, implementing contractile motors dramatically alters chromatin distribution across all three crosslink profiles. Uniform and inverted crosslink profiles lead to higher chromatin accumulation in the nuclear interior, with the inverted profile showing preferentially higher interior accumulation compared to the uniform profile. Strikingly, the linear crosslink profile results in significantly higher chromatin accumulation at the nuclear boundary (Fig. 2d). This chromatin density profile resembles the conventional spatial distribution of chromatin observed in many differentiated cells [3, 5] in that denser heterochromatin-like regions are near the nuclear periphery while less dense euchromatin-like chromatin is localized in the interior.

We also compare the spatial variation of chromatin density in the presence of motors to that in the corresponding passive system by examining the chromatin density scaled by the passive case, given as $\frac{\phi_c^{f_m\neq 0}}{\phi_c^{f_m=0}}$ (insets in Fig. 2c,d), where $\phi_c^{f_m\neq 0}$ and $\phi_c^{f_m=0}$ denote the chromatin densities with and without (passive case) motor activity, respectively. This reveals that extensile motors generally lead to chromatin decompaction, whereas contractile motors result in significant chromatin compaction, particularly in the case of a linear crosslink profile. Our simulations demonstrate that motor activity, combined with nonuniformity in the spatial distribution of crosslinks, can alter the spatial distribution of chromatin. In particular, the synergistic action of contractile motors and a linearly increasing radial profile of crosslinks is sufficient to recapitulate the conventional nuclear architecture, suggesting a novel biophysical mechanism for the establishment of chromatin segregation patterns *in vivo*.

Subsequently, we examine how chromatin distribution changes for different total number, N_c, of crosslinks in the system, while maintaining a linear crosslink profile. Fig. 3 illustrates the effects across passive, extensile, and contractile motor conditions. Our findings reveal that chromatin compaction intensifies with increasing crosslink numbers, N_c, irrespective of motor activity. However, the magnitude of this effect varies markedly between different motor types. The passive and extensile cases (Fig. 3a,b) demonstrate modest enhancement in chromatin density as N_c increases, whereas the contractile case (Fig. 3c) manifests substantially greater chromatin compaction. Among all three cases, extensile motors yield the least chromatin compaction because their activity locally expands chromatin. The absence of motor activity enables intermediate levels of compaction with increasing N_c, as expected from entropic considerations. Contractile motors induce the highest degree of overall chromatin compaction. Notably, the chromatin density is significantly enhanced at the nuclear periphery, reinforcing the conventional chromatin distribution pattern observed in experiments [3, 5]. Additionally, increasing the number of chromatin-lamina linkages reinforces the spatial variation of chromatin density, leading to reduced density in the nuclear interior and accumulation near the periphery (Fig. S4). Our results establish that motor activity can focus spatial inhomogeneities in crosslinking into spatial patterning of chromatin polymer density. Contractile motor activity dramatically amplifies crosslink-dependent peripheral compaction, suggesting a general physical mechanism for regulating chromatin architecture through the interplay of molecular motors with the physical constraints on chromatin in the nucleus.

B. Spatial segregation of euchromatin and heterochromatin contributes to overall chromatin density patterns

To quantify the observed patterns of chromatin architecture in our model, we sought to identify euchromatin-like and heterochromatin-like contributions to the spatial

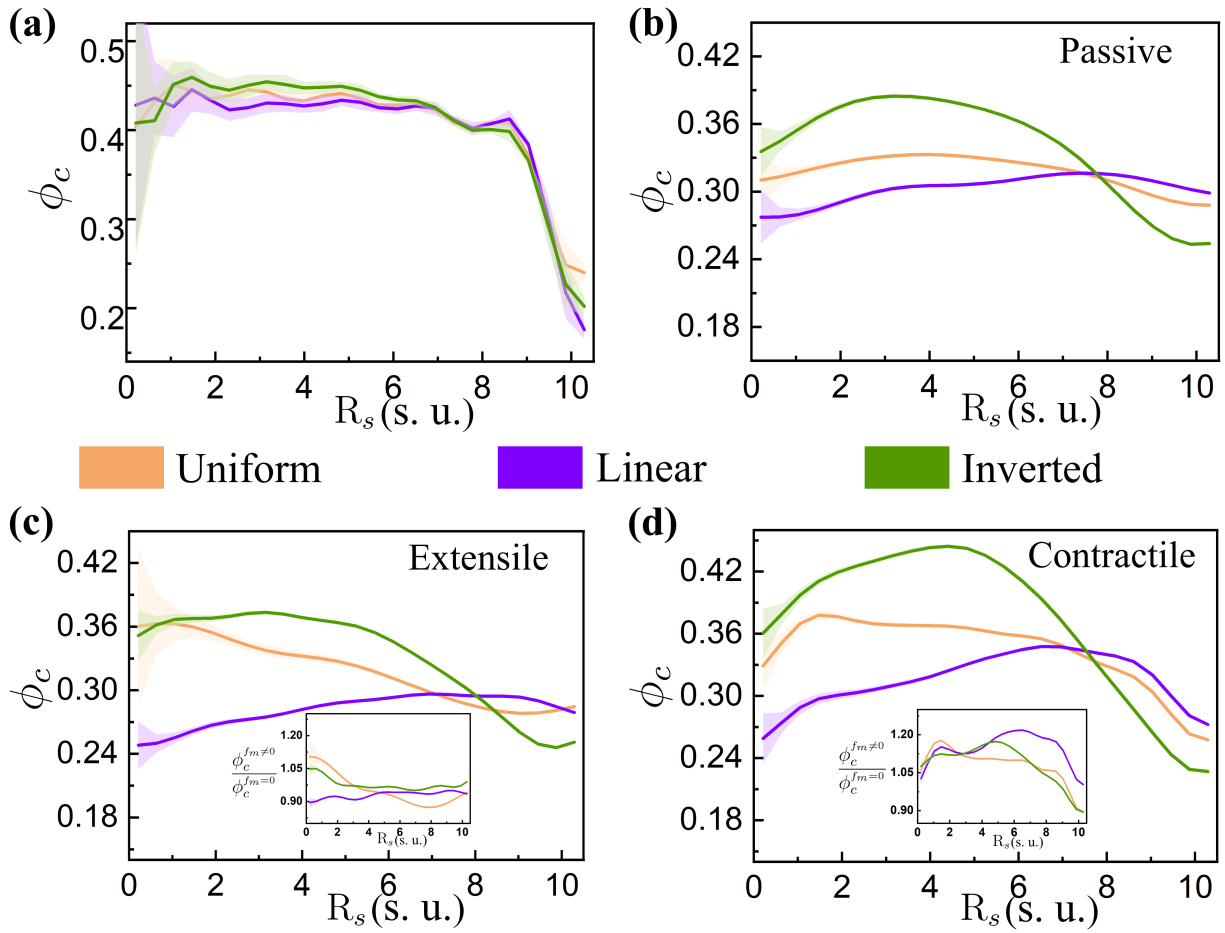


Fig. 2: *Radial chromatin density shaped by motors and crosslink profiles.* Chromatin density, ϕ_c, as a function of R_s. (a) Initial chromatin density at $t = 0$, and final chromatin density for (b) passive, (c) extensile, and (d) contractile motors, for different crosslink density profiles. The rescaled chromatin density, $\frac{\phi_c^{fm\neq 0}}{\phi_c^{fm=0}}$, is shown in the insets of panels (c) and (d), highlighting motor-induced changes relative to the passive case. Each case corresponds to $N_c = 2000$ crosslinks and $N_L = 600$ chromatin-lamina linkages. All quantities are reported in simulation units (s. u.), where 1 s. u. of length = 1 μm and 1 s. u. of time = 0.5 s.

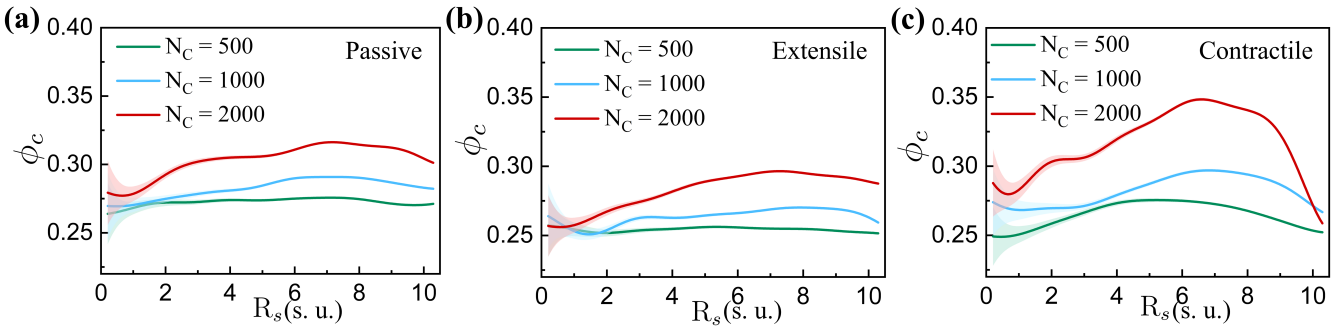


Fig. 3: *Influence of motor activity and number of crosslinks on chromatin distribution.* Chromatin density, ϕ_c, as a function of R_s for (a) passive, (b) extensile, and (c) contractile motors, shown for different numbers of crosslinks (N_c) with a linear crosslink density profile. Results correspond to $N_L = 600$ chromatin crosslinks. All quantities are reported in simulation units (s. u.), where 1 s. u. of length = 1 μm and 1 s. u. of time = 0.5 s.

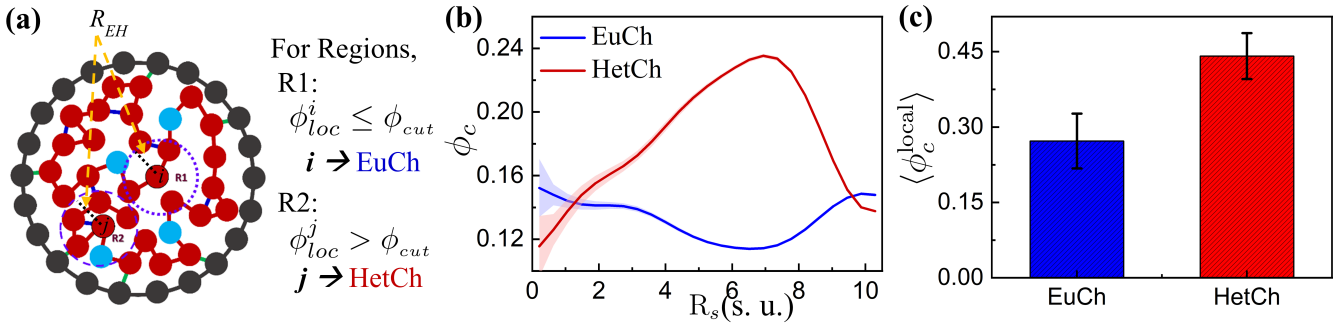


Fig. 4: *Contractile motor-induced organization of euchromatin and heterochromatin.* (a) Schematic illustrating the categorization of chromatin monomers into euchromatin (EuCh) and heterochromatin (HetCh) based on a local density cutoff ($\phi^{i/j}_{loc}$). (b) Density of EuCh and HetCh as a function of R_s and (c) average local density ($\langle \phi_c^{\text{local}} \rangle$) of EuCh and HetCh for a contractile motor with a linear crosslink density profile. The results shown correspond to $N_c = 2000$ crosslinks and $N_L = 600$ chromatin-lamina linkages. All quantities are reported in simulation units (s. u.), where 1 s. u. of length = 1 μm and 1 s. u. of time = 0.5 s.

distribution of chromatin density. We focused on the simulations employing linear crosslink profiles with contractile motors, as this conditions generates chromatin distributions that most closely resemble conventional chromatin organization [3, 5].

To differentiate the radial chromatin density into euchromatin and heterochromatin components, we classified chromatin loci by local chromatin density. For each chromatin monomer i, we compute the local density ϕ^i_{loc} within a spherical volume of cutoff radius R_{EH} centered on that monomer (Fig. 4a). Monomers with $\phi^i_{loc} > \phi_{cut}$ (where ϕ_{cut} represents 95% of the total chromatin density) are categorized as heterochromatin (HetCh), while the remaining monomers are classified as euchromatin (EuCh) (Fig. 4a). The resulting density profiles of heterochromatin and euchromatin with a linear crosslink configuration are plotted as a function of the nuclear radius, R_s, in Fig. 4b, revealing distinct, spatially segregated chromatin domains. We observe that heterochromatin is preferentially localized at the nuclear periphery, while euchromatin predominantly occupies the nuclear interior, a spatial arrangement that aligns with previously reported chromatin organization patterns [3, 5]. In contrast to the contractile motor scenario, the passive and extensile cases exhibit a radial chromatin density profile that is predominantly shaped by euchromatin, with heterochromatin contributing less to the overall density throughout the nucleus (Fig. S5). This highlights that the interplay between crosslink distribution and motor activity could be a fundamental mechanism driving the characteristic spatial segregation and differential compaction of euchromatin and heterochromatin domains in the cell nucleus.

To further assess spatial chromatin compartmentalization, we compute the mean local densities of euchromatin and heterochromatin, $\langle \phi^c_{\text{local}} \rangle$. The average local densities are $\langle \phi^c_{\text{local}}(E) \rangle \approx 0.27$ for euchromatin and $\langle \phi^c_{\text{local}}(H) \rangle \approx 0.44$ for heterochromatin (Fig. 4c). The resulting density ratio, $\frac{\langle \phi^c_{\text{local}}(H) \rangle}{\langle \phi^c_{\text{local}}(E) \rangle} \approx 1.6$, quantifies the degree of chromatin compaction, which is aligned with experimental reports of a 50% density increase in heterochromatin relative to euchromatin [6].

We next characterize the dynamics of the euchromatin and heterochromatin using mean square displacement of monomers, defined as $\overline{\Delta r_i^2(\tau)} = \frac{1}{T'-\tau} \int_0^{T'-\tau} [\mathbf{r}_i(t+\tau) - \mathbf{r}_i(t)]^2 dt$, where $\mathbf{r}_i(t)$ denotes the position of the i^{th} monomer at time t, T' is the total run time, and τ is the lag time (i.e., the time window over which displacements are averaged along a trajectory). To obtain the time-and-ensemble-averaged MSD, we compute the average, $\left\langle \overline{\Delta r^2(\tau)} \right\rangle = \frac{1}{N'} \sum_{i=1}^{N'} \overline{\Delta r_i^2(\tau)}$, where N' represents the number of independent trajectories. We observe that euchromatin displays slightly faster dynamics than heterochromatin (Fig. S6), aligning with the trends noted in prior numerical [33, 76] and experimental [77–79] studies.

C. Radial distribution of motors and the associated number of crosslinks per motor regulate chromatin compaction

The 3D structure of chromatin within the nucleus in our simulations arises from the interplay between mechanical constraints imposed by crosslinks and active, motor-driven processes that dynamically reorganize chromatin. To understand how motor forces and structural connectivity influence chromatin compaction and spatial arrangement, we characterize the radial distribution of motors and the density distribution of crosslinks that they establish throughout the nuclear volume.

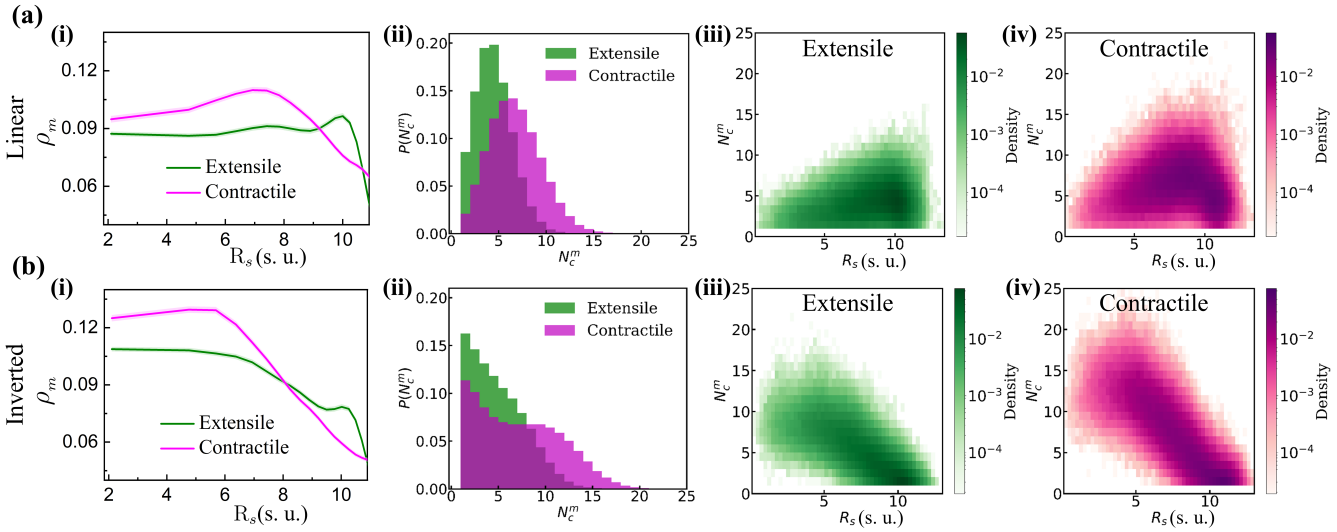


Fig. 5: *Distribution of motor density and motor–crosslink associations for linear and inverted crosslink profiles.* Radial distribution of (i) motor density (ρ_m) and (ii) the average number of crosslinks per motor. Density color map of the number of crosslinks per motor (N_c^m) as a function of R$_s$ for (iii) extensile and (iv) contractile motors. (a) Linear and (b) inverted crosslink profiles, each with subpanels (i–iv). The results shown correspond to $N_c = 2000$ crosslinks and $N_L = 600$ chromatin-lamina linkages. All quantities are reported in simulation units (s. u.), where 1 s. u. of length = 1 μm and 1 s. u. of time = 0.5 s.

We calculate the radial distribution of motors, ρ_m, and number of crosslinks per motor, N_c^m, followed by the density mapping of N_c^m as a function of R_s for linear crosslink profile. We compare this with the inverted crosslink profile, as these represent two extreme cases of spatial crosslink distribution within the nucleus, to identify the critical role of crosslink-motor interplay, as displayed in Fig. 5. To estimate ρ_m, the nuclear volume is divided into concentric spherical shells of equal volume, starting from the center and extending to the nuclear boundary. At each time frame, the center of the nucleus is determined by calculating the mean position of the nuclear lamina particles, and the distance of each motor from this center is measured. The number of motors in each shell is then normalized by the volume of the respective shell, providing a measure of motor density as a function of radial distance, visualized in Fig. 5(a, b)(i). To quantify N_c^m, for each motor monomer, we examine its local environment within a cutoff spherical volume of radius $3r_p$ (r_p is the radius of chromatin monomers) and count the number of crosslinked chromatin monomers within this sphere. This approach provides a direct measure of the average local crosslinking density, P(N_c^m), associated with each motor (Fig. 5(a, b)(ii)). Furthermore, to understand the spatial dependence of crosslinks per motor, we map N_c^m as a function of R_s by binning motors according to their distance from the nuclear center and calculating the number of crosslinks per motor within each radial bin. This analysis reveals how crosslinking density varies across the nuclear volume and correlates with motor distribution patterns (Fig. 5a,b(iii-iv)).

The radial distribution of motor density, ρ_m, reveals distinct spatial organization patterns for extensile and contractile motors depending on the crosslink density profile. For a linear crosslink profile, extensile motors show a relatively uniform density with a slight peripheral increase, whereas contractile motors peak in the outer regions and drop near the boundary (Fig. 5a(i)). On the other hand, for an inverted crosslink profile, both motor types are enriched in the nuclear interior and decrease toward the periphery, with contractile motors exhibiting higher densities than extensile motors across R_s (Fig. 5b(i)). These motor distribution patterns correlate with the overall chromatin density distribution (Fig. 2c,d), suggesting a strong coupling between motor localization and chromatin organization. Analysis of N_c^m distributions uncovers striking differences between the two crosslink cases. In the linear case, contractile motors show a marked increase in crosslinks per motor compared to extensile motors, evident from the rightward shift of the P(N_c^m) peak (Fig. 5a(ii)). Conversely, the inverted crosslink case maintains a consistent peak location for both extensile and contractile motors, with the disparity between them nearly diminished (Fig. 5b(ii)).

The density map further substantiates these observations, demonstrating that motors with the highest number of crosslinks are predominantly localized to the nuclear periphery in the linear crosslink profile when contractile motors are present (Fig. 5a(iii, iv)). This pattern is opposite in the inverted crosslink configuration, where motors with higher crosslink densities are not only fewer

in number but also distributed towards the nuclear interior (Fig. 5b(iii, iv)). These findings underscore the biophysical mechanism by which the linear crosslink profile, coupled with contractile motor activity, promotes chromatin compaction and heterochromatin formation at the nuclear periphery. Contractile motors locally reinforce crosslink density, restricting chromatin mobility and facilitating the formation of dense chromatin domains. This process drives the segregation of heterochromatin at the periphery, while euchromatin remains enriched at the nuclear interior.

To examine the coupling between motor localization and chromatin density, we generated 2D colormaps of local chromatin density, $\phi^c_{\rm loc}$, as a function of nuclear radius (R_s) and local crosslink number per motor (N^m_c). For each motor, R_s, N^m_c, and $\phi^c_{\rm loc}$ were computed within a local neighborhood, and the resulting data were used to construct colormaps for both extensile and contractile motors for linear and inverted crosslink profiles. In the linear crosslink profile, chromatin density increases with N^m_c, particularly in the outer nuclear regions. Contractile motors exhibit stronger compaction–reflected by higher $\phi^c_{\rm loc}$–towards the peripheral nuclear regions with increased N^m_c, consistent with their role in promoting local chromatin compaction (Fig. 6(a, b)). For the inverted crosslink profile (bottom row), the density distribution shifts toward the nuclear interior, consistent with higher crosslink concentration near the center. Motors with higher N^m_c again associate with locally compact chromatin, but this effect is more localized to the central region. This spatial dependence highlights the interplay between radial crosslink patterning, motor localization, and local chromatin organization (Fig. 6(d, e)).

Consistent with the above findings, snapshots of the local neighborhoods surrounding contractile and extensile motors with maximum and minimum crosslinks for both linear (Fig. 6c) and inverted crosslink profile (Fig. 6f) strongly support our observations. Contractile motors with the maximum number of crosslinks exhibit the highest local crowding of chromatin (Fig. 6c(iii), while extensile motors with minimal crosslinks display a significantly sparse local environment (Fig. 6c(ii). Interestingly, contractile motors with the fewest crosslinks can form densely packed regions (Fig. 6c(iv)), comparable to the local chromatin density observed around extensile motors with the highest number of crosslinks (Fig. 6c(i)). Notably, this densification is more pronounced in the linear crosslink profile, highlighting the interplay of crosslink architecture and motor activity.

D. Nuclear deformation enhances peripheral chromatin compaction

Chromatin localization at the nuclear periphery is closely linked to changes in nuclear shape, as reported in earlier studies [50, 64, 66, 69, 80–82]. Dynamic deformations of the nuclear envelope, together with interactions between chromatin and the nuclear lamina, play a key role in regulating peripheral chromatin compaction. Hence, we quantitatively analyze the shape fluctuations of the soft nuclear lamina in our model. We characterize these fluctuations by measuring local geometric deviations from sphericity and computing the power spectrum of surface undulations (Fig. S7). For each time frame, the center of mass of the nuclear lamina is first determined, along with the average radius ($\langle R_s \rangle$) by measuring the mean distance of all lamina monomers from this center. Local deformations are then classified into two distinct types: outward protrusions, referred to as bulges, and inward indentations, termed as wrinkles. To distinguish these deformation types on the three-dimensional lamina surface, regions containing groups of three or more lamina monomers are traced by calculating their radial deviations from $\langle R_s \rangle$. Deformations are classified based on a threshold of 10% deviation from the average radius. Contiguous regions exceeding this threshold are identified as bulges if the deviation is positive, and as wrinkles if it is negative. To quantify the mechanical response of the deformed regions, we evaluate the local fluctuations for both bulges and wrinkles. Local positional fluctuations are quantified as the standard deviation of distances from each monomer in the bulges or wrinkles to their respective local center of mass. The parameter $\delta_{\rm local}$ is defined as the inverse of the squared fluctuations. Higher values of $\delta_{\rm local}$ indicate regions with smaller deformations. Over long times, larger $\delta_{\rm local}$ suggests greater local resistance to deformation, and therefore stiffer areas of the nuclear periphery, while lower values may correspond to more flexible regions.

In Fig. 7, we plot the time evolution profile for the number of deformations, the chromatin density at these deformation sites, and the local fluctuations, $\delta_{\rm local}$, associated with the bulges/wrinkles for the linear crosslink case. The temporal analysis of N_{Def} reveals that contractile motors induce higher fluctuations and a greater number of wrinkles compared to extensile motors, which exhibit fewer deformations (Fig. 7a). Furthermore, the polymer concentration at these deformation sites indicate a preferential localization of chromatin within the wrinkles rather than the bulges (Fig.7b). This observation is supported by the inverse squared fluctuations over time, where wrinkles consistently exhibit larger $\delta_{\rm local}$, suggesting higher stiffness compared to bulges (Fig. 7c). The increased stiffness of the wrinkles is consistent with prior experimental investigations of the mechanical response of the cell nucleus to external forces, which found that nuclear envelope restructuring characterized by wrinkle

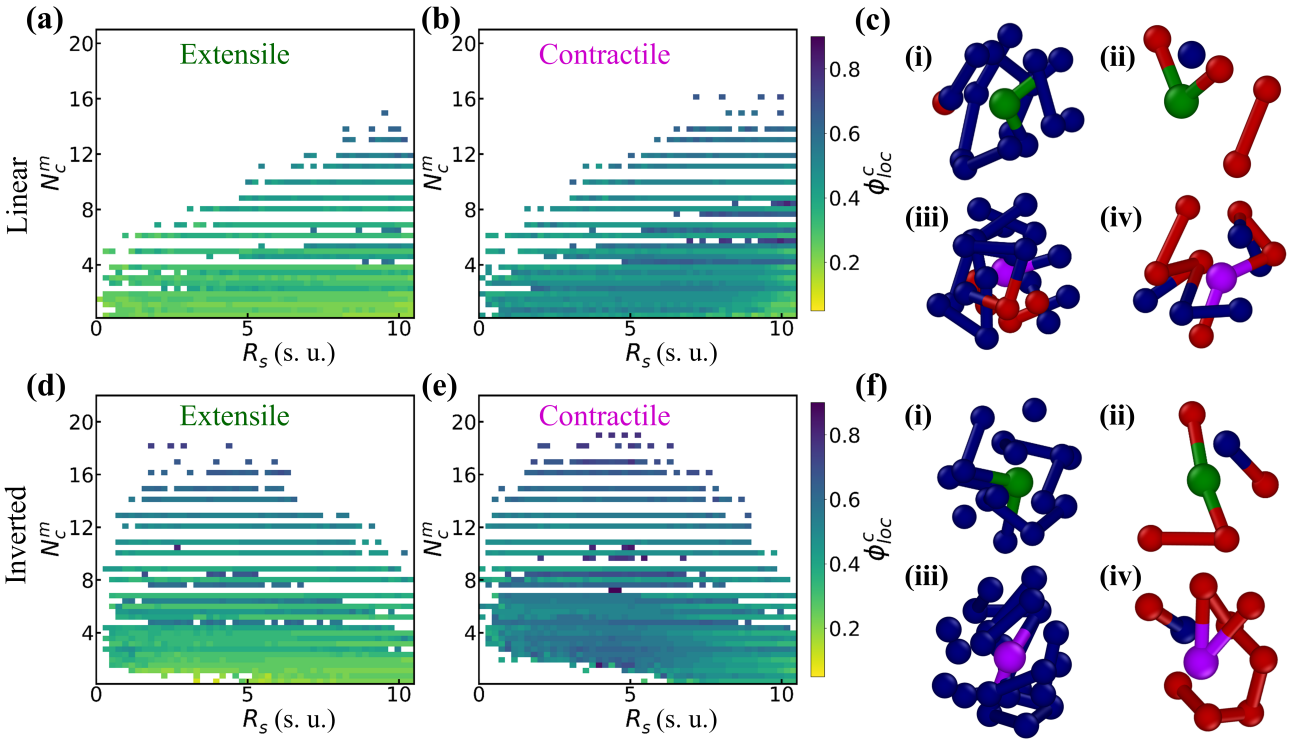


Fig. 6: *Motor–crosslink coupling modulates local chromatin density for linear and inverted crosslink profiles.* Colormap of local chromatin density (ϕ_{loc}^c) as a function of nuclear radius (R_s) and number of crosslinks per motor (N_c^m) for extensile and contractile motors for linear (top row: a, b) and inverted (bottom row: d, e) crosslink profiles. The color bar represents the normalized local chromatin density. Panels (c) and (f) show the local neighborhoods of an extensile motor (i, ii) and a contractile motor (iii, iv), with maximum and minimum crosslinks, respectively, for linear (top row) and reverse (bottom row) profiles. Magenta/green: contractile/extensile motors; blue: crosslinked chromatin; red: chromatin monomers. All quantities are reported in simulation units (s. u.), where 1 s. u. of length = 1 μm and 1 s. u. of time = 0.5 s.

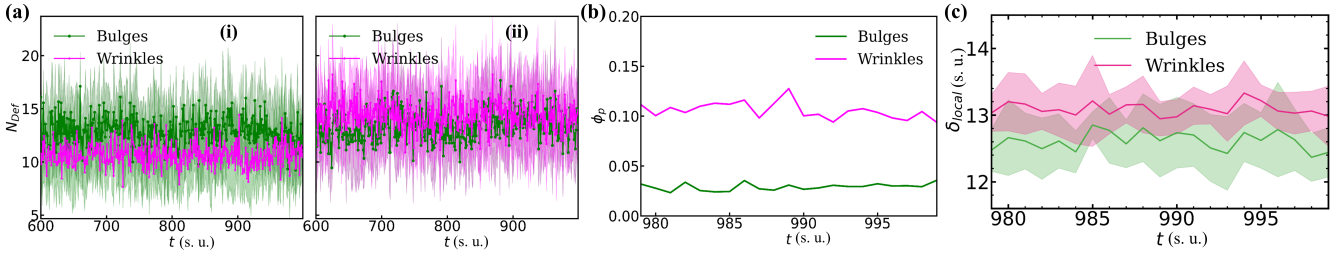


Fig. 7: *Temporal profile of nuclear deformations and local properties of bulges and wrinkles with motor activity for a linear crosslink profile.* Time evolution of (a) the number of bulges/wrinkles (N_{def}) for (i) extensile and (ii) contractile motors, (b) chromatin density (ϕ_p) at bulges/wrinkles, and (c) local fluctuations (δ_{local}) characterizing bulges and wrinkle regions, all for a linear crosslink density profile. The results shown correspond to $N_c = 2000$ crosslinks and $N_L = 600$ chromatin-lamina linkages. All quantities are reported in simulation units (s. u.), where 1 s. u. of length = 1 μm and 1 s. u. of time = 0.5 s.

unfolding is associated with instantaneous stiffening of the nucleus under applied indentation [64].

IV. DISCUSSION

We have analyzed how crosslink distribution and motor activity collectively influence chromatin spatial organization, promoting preferential peripheral heterochromatin formation and resulting in a spatially segregated archi-

tecture resembling conventional nuclear organization. This behavior is captured by our computational model, in which the lamina is represented as a soft deformable sphere and chromatin as a crosslinked polymer chain tethered randomly to the lamina, with dynamic motor proteins driving emergent chromatin compartmentalization. Each motor operates on a characteristic timescale, analogous to molecular motors observed *in vivo*, after which it relocates to a different site along the chromatin chain. The interplay between spatial confinement imposed by crosslinks and the coherent, highly correlated local dynamics driven by motor proteins can either facilitate or hinder genomic interactions. The spatial distribution of crosslinks within the nuclear volume plays a critical role in regulating both the location and degree of chromatin compaction. Contractile motors further amplify this effect by promoting the formation of dense chromatin domains, particularly near the nuclear periphery. Additionally, wrinkling deformations of the nuclear lamina are correlated with accumulating chromatin at the boundary, which could self-reinforce peripheral organization.

Our study of chromatin organization using uniform, linear, and inverted spatial crosslink profiles reveal that a linear crosslink pattern, combined with contractile motor activity, leads to differential chromatin density– euchromatin predominantly localizes to the interior, while heterochromatin accumulates at the periphery. A local density-based classification approach, which maps individual densities of heterochromatin and euchromatin within the nucleus, further verifies this spatial compartmentalization, indicating an approximate 50% difference in density between these two, consistent with experimentally reported values [6, 7]. The dynamic motors employed in our *in silico* approach reveal that contractile motors markedly elevate the number of crosslinks per motor in their vicinity, resulting in strongly constrained local chromatin motion relative to extensile motors. This leads to the formation of high-density chromatin domains and mediating heterochromatin accumulation. Notably, this effect is most pronounced with the linear crosslink profile, where contractile motors with an increased number of crosslinks nearby are predominantly concentrated at the nuclear periphery, facilitating peripheral heterochromatin formation. In contrast, uniform and inverted crosslink profiles exhibit fewer motors with a higher number of crosslinks in their respective local environments, and when such motors are present, they are only marginally localized near the periphery.

The soft nuclear lamina exhibits shape fluctuations, as reported in previous studies [48, 49, 63, 64, 69, 83], and these deformations can give rise to the formation of bulges and wrinkles [64]. Wrinkles formed in the presence of contractile motors exhibit greater stiffness than bulges, which is directly correlated with a higher local concentration of chromatin near the wrinkles. Taken together, these findings suggest that a complete phase segregation into distinct low- and high-density chromatin regions is not strictly necessary to produce the conventional pattern of differential chromatin density observed in the nucleus. More importantly, our study indicates that local spatial effects driven by crosslink arrangement and motor activity are sufficient to establish the characteristic positioning of heterochromatin and euchromatin.

To experimentally validate our model's predictions on the role of spatially patterned crosslinks and motor activity in shaping nuclear chromatin organization, we propose combining high-resolution chromatin imaging with genetic perturbations. Crosslink distribution can be visualized via immunofluorescence of endogenous proteins, such as HP1α/γ, that crosslink chromatin and mark heterochromatin-associated domains [6, 84]. Crosslink density can be modulated by tuning HP1 expression levels: overexpression could promote chromatin crosslinking via HP1 oligomerization espeically in H3K9me3-enriched regions, while depletion or mutation would reduce crosslink formation [11, 12, 57, 85]. Spatially patterned crosslinking could potentially be genetically engineered through synthetic recruitment of HP1 to defined genomic loci [86, 87] or optogenetically induced clustering [88, 89], enabling spatial modulation of local crosslink density. Motor activity may be experimentally modulated by altering ATP availability or treating with inhibitors of transcription and other active processes [40]. Locus tracking [42, 90] can assess the dynamic impact of crosslinks and motors. Together, these approaches would provide a versatile framework to test the mechanistic hypotheses emerging from our simulations.

V. ACKNOWLEDGMENTS

This research was supported in part through computational resources provided by Syracuse University. EJB acknowledges support from the NIH Common Fund 4D Nucleome Program (UM1HG011536). JMS acknowledges funding support form from the National Science Foundation under grant DMR-2204312.

[1] T. Misteli, The self-organizing genome: principles of genome architecture and function, Cell **183**, 28 (2020).

[2] Y. Kalukula, A. D. Stephens, J. Lammerding, and S. Gabriele, Mechanics and functional consequences of

nuclear deformations, Nat. Rev. Mol. Cell Biol. **23**, 583 (2022).
[3] I. Solovei, K. Thanisch, and Y. Feodorova, How to rule the nucleus: divide et impera, Curr. Opin. Cell Biol. **40**, 47 (2016).
[4] J. Dekker and L. A. Mirny, The chromosome folding problem and how cells solve it, Cell **187**, 6424 (2024).
[5] I. Solovei, M. Kreysing, C. Lanctôt, S. Kösem, L. Peichl, T. Cremer, J. Guck, and B. Joffe, Nuclear architecture of rod photoreceptor cells adapts to vision in mammalian evolution, Cell **137**, 356 (2009).
[6] R. Imai, T. Nozaki, T. Tani, K. Kaizu, K. Hibino, S. Ide, S. Tamura, K. Takahashi, M. Shribak, and K. Maeshima, Density imaging of heterochromatin in live cells using orientation-independent-DIC microscopy, Mol. Biol. Cell **28**, 3349 (2017).
[7] H. D. Ou, S. Phan, T. J. Deerinck, A. Thor, M. H. Ellisman, and C. C. O'shea, Chromemt: Visualizing 3d chromatin structure and compaction in interphase and mitotic cells, Science **357**, eaag0025 (2017).
[8] M. Barbieri, M. Chotalia, J. Fraser, L.-M. Lavitas, J. Dostie, A. Pombo, and M. Nicodemi, Complexity of chromatin folding is captured by the strings and binders switch model, Proc. Natl. Acad. Sci. USA **109**, 16173 (2012).
[9] D. Jost, P. Carrivain, G. Cavalli, and C. Vaillant, Modeling epigenome folding: formation and dynamics of topologically associated chromatin domains, Nucleic Acids Res. **42**, 9553 (2014).
[10] M. Di Pierro, B. Zhang, E. L. Aiden, P. G. Wolynes, and J. N. Onuchic, Transferable model for chromosome architecture, Proc. Natl. Acad. Sci. USA **113**, 12168 (2016).
[11] A. G. Larson, D. Elnatan, M. M. Keenen, M. J. Trnka, J. B. Johnston, A. L. Burlingame, D. A. Agard, S. Redding, and G. J. Narlikar, Liquid droplet formation by HP1α suggests a role for phase separation in heterochromatin, Nature **547**, 236 (2017).
[12] A. R. Strom, A. V. Emelyanov, M. Mir, D. V. Fyodorov, X. Darzacq, and G. H. Karpen, Phase separation drives heterochromatin domain formation, Nature **547**, 241 (2017).
[13] S. S. Rao, S.-C. Huang, B. G. St Hilaire, J. M. Engreitz, E. M. Perez, K.-R. Kieffer-Kwon, A. L. Sanborn, S. E. Johnstone, G. D. Bascom, I. D. Bochkov, *et al.*, Cohesin loss eliminates all loop domains, Cell **171**, 305 (2017).
[14] J. Nuebler, G. Fudenberg, M. Imakaev, N. Abdennur, and L. A. Mirny, Chromatin organization by an interplay of loop extrusion and compartmental segregation, Proc. Natl. Acad. Sci. USA **115**, E6697 (2018).
[15] M. Falk, Y. Feodorova, N. Naumova, M. Imakaev, B. R. Lajoie, H. Leonhardt, B. Joffe, J. Dekker, G. Fudenberg, I. Solovei, *et al.*, Heterochromatin drives compartmentalization of inverted and conventional nuclei, Nature **570**, 395 (2019).
[16] B. A. Gibson, L. K. Doolittle, M. W. Schneider, L. E. Jensen, N. Gamarra, L. Henry, D. W. Gerlich, S. Redding, and M. K. Rosen, Organization of chromatin by intrinsic and regulated phase separation, Cell **179**, 470 (2019).
[17] L. Wang, Y. Gao, X. Zheng, C. Liu, S. Dong, R. Li, G. Zhang, Y. Wei, H. Qu, Y. Li, *et al.*, Histone modifications regulate chromatin compartmentalization by contributing to a phase separation mechanism, Mol. Cell **76**, 646 (2019).
[18] S. Sanulli, M. Trnka, V. Dharmarajan, R. Tibble, B. Pascal, A. Burlingame, P. Griffin, J. Gross, and G. Narlikar, HP1 reshapes nucleosome core to promote phase separation of heterochromatin, Nature **575**, 390 (2019).
[19] D. Amiad-Pavlov, D. Lorber, G. Bajpai, A. Reuveny, F. Roncato, R. Alon, S. Safran, and T. Volk, Live imaging of chromatin distribution reveals novel principles of nuclear architecture and chromatin compartmentalization, Sci. Adv. **7**, eabf6251 (2021).
[20] O. Adame-Arana, G. Bajpai, D. Lorber, T. Volk, and S. Safran, Regulation of chromatin microphase separation by binding of protein complexes, eLife **12**, e82983 (2023).
[21] L. A. Mirny, M. Imakaev, and N. Abdennur, Two major mechanisms of chromosome organization, Curr. Opin. Cell Biol. **58**, 142 (2019).
[22] G. Bajpai, D. Amiad Pavlov, D. Lorber, T. Volk, and S. Safran, Mesoscale phase separation of chromatin in the nucleus, eLife **10**, e63976 (2021).
[23] A. G. Attar, J. Paturej, E. J. Banigan, and A. Erbaş, Chromatin phase separation and nuclear shape fluctuations are correlated in a polymer model of the nucleus, Nucleus **15**, 2351957 (2024).
[24] S. Ghosh, V. C. Cuevas, B. Seelbinder, and C. P. Neu, Image-based elastography of heterochromatin and euchromatin domains in the deforming cell nucleus, Small **17**, 2006109 (2021).
[25] P. R. Cook and D. Marenduzzo, Entropic organization of interphase chromosomes, J. Cell Biol. **186**, 825 (2009).
[26] A. Brunet, N. Destainville, and P. Collas, Physical constraints in polymer modeling of chromatin associations with the nuclear periphery at kilobase scale, Nucleus **12**, 6 (2021).
[27] M. Girard, M. O. De La Cruz, J. F. Marko, and A. Erbaş, Heterogeneous flexibility can contribute to chromatin segregation in the cell nucleus, Phys. Rev. E **110**, 014403 (2024).
[28] C. A. Brackley, S. Taylor, A. Papantonis, P. R. Cook, and D. Marenduzzo, Nonspecific bridging-induced attraction drives clustering of DNA-binding proteins and genome organization, Proc. Natl. Acad. Sci. USA **110**, E3605 (2013).
[29] C. A. Brackley, J. Johnson, S. Kelly, P. R. Cook, and D. Marenduzzo, Simulated binding of transcription factors to active and inactive regions folds human chromosomes into loops, rosettes and topological domains, Nucleic Acids Res. **44**, 3503 (2016).
[30] N. Ganai, S. Sengupta, and G. I. Menon, Chromosome positioning from activity-based segregation, Nucleic Acids Res. **42**, 4145 (2014).
[31] A. Y. Grosberg and J.-F. Joanny, Nonequilibrium statistical mechanics of mixtures of particles in contact with different thermostats, Phys. Rev. E **92**, 032118 (2015).
[32] J. Smrek and K. Kremer, Small activity differences drive phase separation in active-passive polymer mixtures, Phys. Rev. Lett. **118**, 098002 (2017).
[33] L. Liu, G. Shi, D. Thirumalai, and C. Hyeon, Chain organization of human interphase chromosome determines the spatiotemporal dynamics of chromatin loci, PLoS Comput. Biol. **14**, e1006617 (2018).
[34] R. Das, T. Sakaue, G. Shivashankar, J. Prost, and T. Hiraiwa, How enzymatic activity is involved in chromatin organization, eLife **11**, e79901 (2022).

[35] S. Chaki, L. Theeyancheri, and R. Chakrabarti, A polymer chain with dipolar active forces in connection to spatial organization of chromatin, Soft Matter **19**, 1348 (2023).

[36] A. Mahajan, W. Yan, A. Zidovska, D. Saintillan, and M. J. Shelley, Euchromatin activity enhances segregation and compaction of heterochromatin in the cell nucleus, Phys. Rev. X **12**, 041033 (2022).

[37] L. Hilbert, Y. Sato, K. Kuznetsova, T. Bianucci, H. Kimura, F. Jülicher, A. Honigmann, V. Zaburdaev, and N. L. Vastenhouw, Transcription organizes euchromatin via microphase separation, Nat. Commun. **12**, 1360 (2021).

[38] S. Brahmachari, T. Markovich, F. C. MacKintosh, and J. N. Onuchic, Temporally correlated active forces drive segregation and enhanced dynamics in chromosome polymers, PRX Life **2**, 033003 (2024).

[39] A. Goychuk, D. Kannan, A. K. Chakraborty, and M. Kardar, Polymer folding through active processes recreates features of genome organization, Proc. Natl. Acad. Sci. USA **120**, e2221726120 (2023).

[40] A. Zidovska, D. A. Weitz, and T. J. Mitchison, Micron-scale coherence in interphase chromatin dynamics, Proc. Nat. Acad. Sci. U.S.A **110**, 15555 (2013).

[41] H. A. Shaban, R. Barth, and K. Bystricky, Formation of correlated chromatin domains at nanoscale dynamic resolution during transcription, Nucleic Acids Res. **46**, e77 (2018).

[42] N. Khanna, Y. Zhang, J. S. Lucas, O. K. Dudko, and C. Murre, Chromosome dynamics near the sol-gel phase transition dictate the timing of remote genomic interactions, Nat. Commun. **10**, 2771 (2019).

[43] R. Barth, K. Bystricky, and H. Shaban, Coupling chromatin structure and dynamics by live super-resolution imaging, Science advances **6**, eaaz2196 (2020).

[44] H. A. Shaban, R. Barth, L. Recoules, and K. Bystricky, Hi-D: nanoscale mapping of nuclear dynamics in single living cells, Genome Biol. **21**, 95 (2020).

[45] I. Eshghi, J. A. Eaton, and A. Zidovska, Interphase chromatin undergoes a local sol-gel transition upon cell differentiation, Phys. Rev. Lett. **126**, 228101 (2021).

[46] M. Locatelli, J. Lawrimore, H. Lin, S. Sanaullah, C. Seitz, D. Segall, P. Kefer, N. Salvador Moreno, B. Lietz, R. Anderson, *et al.*, DNA damage reduces heterogeneity and coherence of chromatin motions, Proc. Natl. Acad. Sci. USA **119**, e2205166119 (2022).

[47] R. Bruinsma, A. Y. Grosberg, Y. Rabin, and A. Zidovska, Chromatin hydrodynamics, Biophys. J. **106**, 1871 (2014).

[48] F.-Y. Chu, S. C. Haley, and A. Zidovska, On the origin of shape fluctuations of the cell nucleus, Proc. Nat. Acad. Sci. USA **114**, 10338 (2017).

[49] K. Liu, A. E. Patteson, E. J. Banigan, and J. Schwarz, Dynamic nuclear structure emerges from chromatin cross-links and motors, Phys. Rev. Lett. **126**, 158101 (2021).

[50] I. K. Berg, M. L. Currey, S. Gupta, Y. Berrada, B. V. Nguyen, M. Pho, A. E. Patteson, J. Schwarz, E. J. Banigan, and A. D. Stephens, Transcription inhibition suppresses nuclear blebbing and rupture independently of nuclear rigidity, J. Cell Sci. **136**, jcs261547 (2023).

[51] K. Prince, K. Lin, A. Li, N. Borowski, and A. D. Stephens, Transcriptional activity generates chromatin motion that drives nuclear blebbing, bioRxiv , 2025 (2025).

[52] A. Zidovska, The self-stirred genome: large-scale chromatin dynamics, its biophysical origins and implications, Curr. Opin. Genet. Dev. **61**, 83 (2020).

[53] A. Bird, Cohesin as an essential disruptor of chromosome organization, Mol. Cell **85**, 1054 (2025).

[54] D. Canzio, E. Y. Chang, S. Shankar, K. M. Kuchenbecker, M. D. Simon, H. D. Madhani, G. J. Narlikar, and B. Al-Sady, Chromodomain-mediated oligomerization of HP1 suggests a nucleosome-bridging mechanism for heterochromatin assembly, Mol. Cell **41**, 67 (2011).

[55] D. Canzio, A. Larson, and G. J. Narlikar, Mechanisms of functional promiscuity by HP1 proteins, Trends Cell Biol. **24**, 377 (2014).

[56] S. Machida, Y. Takizawa, M. Ishimaru, Y. Sugita, S. Sekine, J.-i. Nakayama, M. Wolf, and H. Kurumizaka, Structural basis of heterochromatin formation by human HP1, Molecular cell **69**, 385 (2018).

[57] A. R. Strom, R. J. Biggs, E. J. Banigan, X. Wang, K. Chiu, C. Herman, J. Collado, F. Yue, J. C. Ritland Politz, L. J. Tait, *et al.*, HP1α is a chromatin crosslinker that controls nuclear and mitotic chromosome mechanics, eLife **10**, e63972 (2021).

[58] V. Sokolova, J. Miratsky, V. Svetlov, M. Brenowitz, J. Vant, T. S. Lewis, K. Dryden, G. Lee, S. Sarkar, E. Nudler, *et al.*, Structural mechanism of HP1α-dependent transcriptional repression and chromatin compaction, Structure **32**, 2094 (2024).

[59] A. Kumar and H. Kono, Heterochromatin protein 1 (HP1): interactions with itself and chromatin components, Biophys. Rev. **12**, 387 (2020).

[60] Y. Yang, R. Liu, R. Qiu, Y. Zheng, W. Huang, H. Hu, Q. Ji, H. He, Y. Shang, Y. Gong, *et al.*, Crl4b promotes tumorigenesis by coordinating with SUV39H1/HP1/DNMT3A in DNA methylation-based epigenetic silencing, Oncogene **34**, 104 (2015).

[61] D. Saintillan, M. J. Shelley, and A. Zidovska, Extensile motor activity drives coherent motions in a model of interphase chromatin, Proc. Natl. Acad. Sci. USA **115**, 11442 (2018).

[62] S. Redding, Dynamic asymmetry and why chromatin defies simple physical definitions, Curr. Opin. Cell Biol. **70**, 116 (2021).

[63] A. E. Patteson, A. Vahabikashi, K. Pogoda, S. A. Adam, K. Mandal, M. Kittisopikul, S. Sivagurunathan, A. Goldman, R. D. Goldman, and P. A. Janmey, Vimentin protects cells against nuclear rupture and DNA damage during migration, J. Cell Biol. **218**, 4079 (2019).

[64] W. Tang, X. Chen, X. Wang, M. Zhu, G. Shan, T. Wang, W. Dou, J. Wang, J. Law, Z. Gong, *et al.*, Indentation induces instantaneous nuclear stiffening and unfolding of nuclear envelope wrinkles, Proc. Nat. Acad. Sci. USA **120**, e2307356120 (2023).

[65] A. Tajik, Y. Zhang, F. Wei, J. Sun, Q. Jia, W. Zhou, R. Singh, N. Khanna, A. S. Belmont, and N. Wang, Transcription upregulation via force-induced direct stretching of chromatin, Nat. Mater. **15**, 1287 (2016).

[66] A. D. Stephens, E. J. Banigan, and J. F. Marko, Chromatin's physical properties shape the nucleus and its functions, Curr. Opin. Cell Biol. **58**, 76 (2019).

[67] M. M. Nava, Y. A. Miroshnikova, L. C. Biggs, D. B. Whitefield, F. Metge, J. Boucas, H. Vihinen, E. Jokitalo, X. Li, J. M. G. Arcos, *et al.*, Heterochromatin-driven nuclear softening protects the genome against mechanical stress-induced damage, Cell **181**, 800 (2020).

[68] C.-R. Hsia, J. McAllister, O. Hasan, J. Judd, S. Lee, R. Agrawal, C.-Y. Chang, P. Soloway, and J. Lammerding, Confined migration induces heterochromatin formation and alters chromatin accessibility, iScience **25** (2022).

[69] H. Liang, Y.-J. Wang, Y. Liu, W. Liu, B. Liu, and Y.-J. Liu, Microtopography-induced nuclear deformation triggers chromatin reorganization and cytoskeleton remodeling, Chem. Biomed. Imaging **2**, 481 (2024).

[70] A. G. Attar, J. Paturej, O. S. Sariyer, E. J. Banigan, and A. Erbas, Peripheral heterochromatin tethering is required for chromatin-based nuclear mechanical response, bioRxiv , 2025 (2025).

[71] Y. A. Miroshnikova and S. A. Wickström, Mechanical forces in nuclear organization, Cold Spring Harb Perspect Biol. **14**, a039685 (2022).

[72] A. D. Stephens, E. J. Banigan, S. A. Adam, R. D. Goldman, and J. F. Marko, Chromatin and lamin A determine two different mechanical response regimes of the cell nucleus, Mol. Biol. Cell **28**, 1984 (2017).

[73] E. J. Banigan, A. D. Stephens, and J. F. Marko, Mechanics and buckling of biopolymeric shells and cell nuclei, Biophys. J. **113**, 1654 (2017).

[74] T. J. Kirby and J. Lammerding, Emerging views of the nucleus as a cellular mechanosensor, Nat. Cell Biol. **20**, 373 (2018).

[75] M. C. Lionetti, S. Bonfanti, M. R. Fumagalli, Z. Budrikis, F. Font-Clos, G. Costantini, O. Chepizhko, S. Zapperi, and C. A. La Porta, Chromatin and cytoskeletal tethering determine nuclear morphology in progerin-expressing cells, Biophys. J. **118**, 2319 (2020).

[76] S. Shinkai, T. Nozaki, K. Maeshima, and Y. Togashi, Dynamic nucleosome movement provides structural information of topological chromatin domains in living human cells, PLoS Comput. Biol. **12**, e1005136 (2016).

[77] K. Minami, K. Nakazato, S. Ide, K. Kaizu, K. Higashi, S. Tamura, A. Toyoda, K. Takahashi, K. Kurokawa, and K. Maeshima, Replication-dependent histone labeling dissects the physical properties of euchromatin/heterochromatin in living human cells, Sci. Adv. **11**, eadu8400 (2025).

[78] N. A. Hathaway, O. Bell, C. Hodges, E. L. Miller, D. S. Neel, and G. R. Crabtree, Dynamics and memory of heterochromatin in living cells, Cell **149**, 1447 (2012).

[79] T. Nozaki, R. Imai, M. Tanbo, R. Nagashima, S. Tamura, T. Tani, Y. Joti, M. Tomita, K. Hibino, M. T. Kanemaki, *et al.*, Dynamic organization of chromatin domains revealed by super-resolution live-cell imaging, Mol. Cell **67**, 282 (2017).

[80] A. Poleshko, K. M. Mansfield, C. C. Burlingame, M. D. Andrake, N. R. Shah, and R. A. Katz, The human protein prr14 tethers heterochromatin to the nuclear lamina during interphase and mitotic exit, Cell Rep. **5**, 292 (2013).

[81] S. M. Schreiner, P. K. Koo, Y. Zhao, S. G. Mochrie, and M. C. King, The tethering of chromatin to the nuclear envelope supports nuclear mechanics, Nat. Commun **6**, 7159 (2015).

[82] A. D. Stephens, P. Z. Liu, E. J. Banigan, L. M. Almassalha, V. Backman, S. A. Adam, R. D. Goldman, and J. F. Marko, Chromatin histone modifications and rigidity affect nuclear morphology independent of lamins, Mol. Biol. Cell **29**, 220 (2018).

[83] S. Talwar, A. Kumar, M. Rao, G. I. Menon, and G. Shivashankar, Correlated spatio-temporal fluctuations in chromatin compaction states characterize stem cells, Biophys. J. **104**, 553 (2013).

[84] B. Bintu, L. J. Mateo, J.-H. Su, N. A. Sinnott-Armstrong, M. Parker, S. Kinrot, K. Yamaya, A. N. Boettiger, and X. Zhuang, Super-resolution chromatin tracing reveals domains and cooperative interactions in single cells, Science **362**, eaau1783 (2018).

[85] S. V. Brasher, B. O. Smith, R. H. Fogh, D. Nietlispach, A. Thiru, P. R. Nielsen, R. W. Broadhurst, L. J. Ball, N. V. Murzina, and E. D. Laue, The structure of mouse HP1 suggests a unique mode of single peptide recognition by the shadow chromo domain dimer, EMBO J. (2000).

[86] K. Ayyanathan, M. S. Lechner, P. Bell, G. G. Maul, D. C. Schultz, Y. Yamada, K. Tanaka, K. Torigoe, and F. J. Rauscher, Regulated recruitment of HP1 to a euchromatic gene induces mitotically heritable, epigenetic gene silencing: a mammalian cell culture model of gene variegation, Genes Dev. **17**, 1855 (2003).

[87] P. J. Verschure, I. Van Der Kraan, W. De Leeuw, J. Van Der Vlag, A. E. Carpenter, A. S. Belmont, and R. Van Driel, In vivo HP1 targeting causes large-scale chromatin condensation and enhanced histone lysine methylation, Mol. Cell. Biol. **25**, 4552 (2005).

[88] Y. Shin, J. Berry, N. Pannucci, M. P. Haataja, J. E. Toettcher, and C. P. Brangwynne, Spatiotemporal control of intracellular phase transitions using light-activated optodroplets, Cell **168**, 159 (2017).

[89] F. Erdel, A. Rademacher, R. Vlijm, J. Tünnermann, L. Frank, R. Weinmann, E. Schweigert, K. Yserentant, J. Hummert, C. Bauer, *et al.*, Mouse heterochromatin adopts digital compaction states without showing hallmarks of HP1-driven liquid-liquid phase separation, Mol. Cell **78**, 236 (2020).

[90] M. Gabriele, H. B. Brandão, S. Grosse-Holz, A. Jha, G. M. Dailey, C. Cattoglio, T.-H. S. Hsieh, L. Mirny, C. Zechner, and A. S. Hansen, Dynamics of CTCF- and cohesin-mediated chromatin looping revealed by live-cell imaging, Science **376**, 496 (2022).

SUPPORTING INFORMATION

1. Computational Model

The chromatin-lamina system is modeled with chromatin represented as a Rouse polymer chain and the nuclear lamina as an elastic, polymeric spherical shell. Linkages are formed between the chromatin and the lamina. The shell consists of 5000 monomers positioned using a Fibonacci sphere algorithm, with each pair of neighboring monomers connected by Hookean springs of spring constant K, forming a mesh with an average coordination number of 4.5. The chromatin is modeled as a Rouse chain with 5000 monomers (N), generated via a three-dimensional self-avoiding random walk on an FCC lattice. Each monomer has a radius $r_p = 0.43089$ and experiences soft-core repulsion to capture excluded volume effects. The lamina monomers share the same physical properties (size and spring strength) as the chromatin monomers. To initialize the system, the chromatin is confined within a spherical shell of radius R$s = 10$. The shell is gradually shrunk by moving lamina monomers inward, which compresses the chromatin via steric interactions. Once the desired radius is reached, spring lengths and monomer positions are adjusted to finalize the initial configuration (Fig. S1). This process is repeated to generate 50 independent initial configurations. Given $r_p = 0.43089$, the packing fraction in the confined shell is approximately $\phi_{\text{pack}} \approx 0.4$ (details of simulation parameters are provided in Table S1).

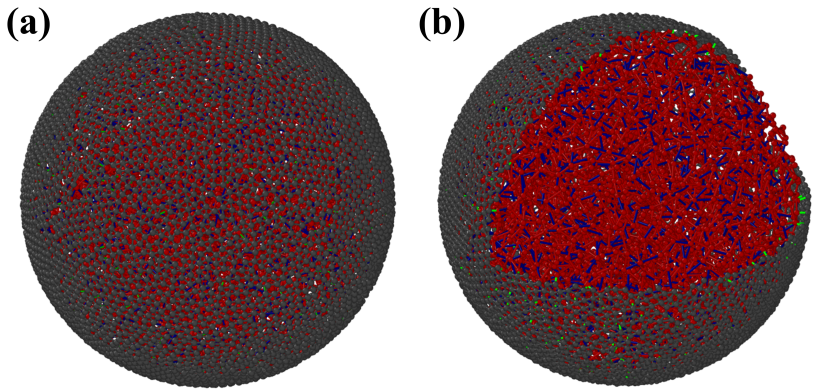


Fig. S1: *Snapshots of the initial configuration of the chromatin–lamina system.* (a) Initial configuration of chromatin confined within the nuclear lamina. (b) Crosslinked chromatin is shown with red beads; crosslinks are depicted in blue, and chromatin-lamina linkages are highlighted in green.

Chromatin crosslinks are introduced by adding N_c springs between randomly selected pairs of chromatin monomers, provided their mutual distance is less than $r_{\text{link}} = 3r_p$. The stiffness of the crosslink springs matches that of the polymer backbone.Motor activity is incorporated by designating N_m chromatin monomers as active. Each active monomer exerts a force $\boldsymbol{F_a} = \pm f_m \hat{r}ij$ on nearby monomers, where f_m denotes the motor force magnitude, and $\hat{r}ij$ is the unit vector between the interacting monomers. We consider two types of motors: extensile, which push monomers apart, and contractile, which draw them together.

2. Simulation Results

2.1. Radius of gyration of chromatin polymer and radial density distribution of chromatin monomers

For a chromatin polymer, the radius of gyration is defined as $R_g = \sqrt{\frac{1}{N}\sum_{i=1}^{N}(\boldsymbol{r}_i - \boldsymbol{r}_{\text{com}})^2}$, where $N = 5000$ is the total number of monomers in the chain, r_i is the position of i^{th} monomer, and r_{com} is the center of mass of the chromatin chain. The radius of the nuclear shell is fixed at $R_s = 10$ considering as an initial hard shell. The soft shell expands in response to thermal fluctuations and the active forces generated by the chromatin chain confined within the nucleus. Fig. S2 shows the average nuclear radius, $\langle R_s \rangle$ (top row, solid lines), and average radius of gyration, $\langle R_g \rangle$, of the chromatin chain (bottom row, dashed lines) as a function of simulation time. Following a short initial expansion, the radii of both the chromatin chain and the nuclear shell reach a plateau by 100τ, indicating the onset of a steady-state configuration.

Parameters	Numerical Value
Number of polymer monomers (N)	5000
Number of shell particles (N_s)	5000
Radius of a polymer monomer (r_p)	0.43089
Radius of a shell particle (r_s)	0.43089
Radius of the hard shell (R_s)	10
Packing fraction (ϕ_{pack})	0.4
Number of crosslinks (N_c)	0, 500, 1000, 2000
Number of linkages (N_L)	0, 50, 250, 600
Number of motors (N_m)	500
Magnitude of motor force (f_m)	10
Motor turnover time scale (τ_m)	20
Harmonic spring constant (K)	140
Excluded volume strength (K_{Ex})	140
Damping (ξ)	1
Simulation timestep ($d\tau$)	10^{-4}
Thermal Energy (K_BT)	1
Diffusion constant (D)	1
Cutoff used for crosslinks (r_{link})	$3\times r_p$
Motor radius (r_{motor})	$1.5\times r_p$

Table S1: Parameters used in the simulations.

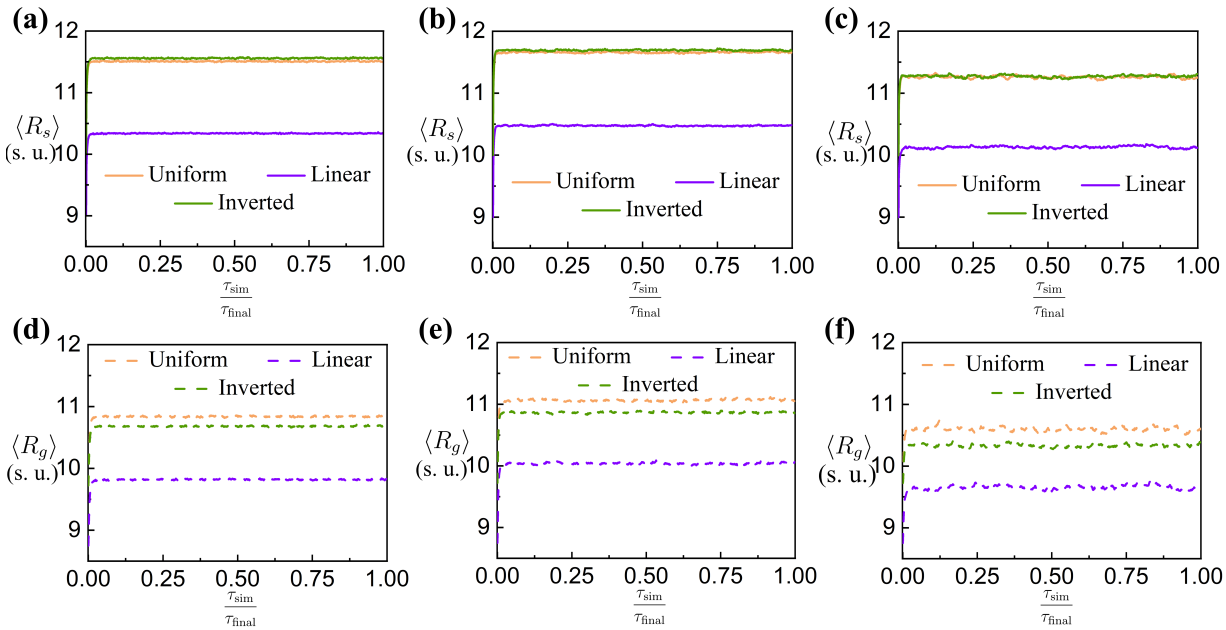


Fig. S2: *Temporal profile of nuclear radius and chromatin radius of gyration for passive, extensile, and contractile motors across different crosslink profiles.* Time evolution of the average radius of the nuclear lamina, $\langle R_s \rangle$ (solid lines, top row), and the chromatin radius of gyration, $\langle R_g \rangle$ (dashed lines, bottom row), for (a) passive, (b) extensile, and (c) contractile motor cases with different crosslink density profiles. The results shown correspond to $N_c = 2000$ crosslinks and $N_L = 600$ chromatin-lamina linkages. All quantities are reported in simulation units (s. u.), where 1 s. u. of length = 1 μm and 1 s. u. of time = 0.5 s.

2.2. Influence of chromatin-lamina linkages on chromatin spatial distribution

We consider a reference case in which both chromatin crosslinks (N_c) and chromatin–lamina linkages (N_L) are absent. The resulting radial chromatin distributions for passive, extensile, and contractile motor cases are shown in Fig. S3a. In the absence of crosslinks and lamina linkages, the chromatin density remains largely uniform across the nuclear radius, R_s. A slight accumulation of chromatin is observed toward the nuclear interior, which becomes more pronounced in the presence of contractile motor activity (Fig. S3a).

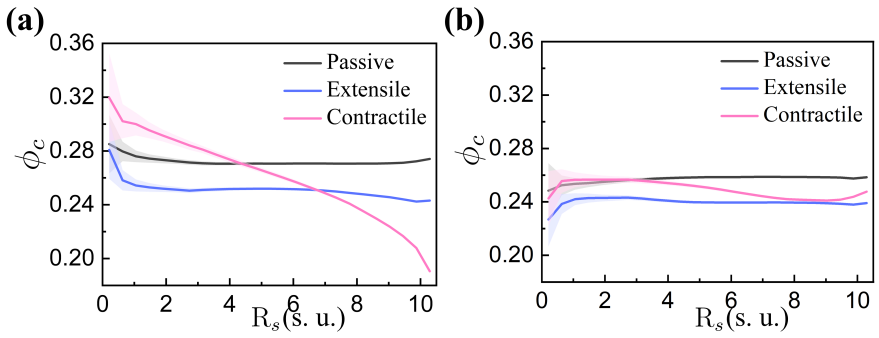


Fig. S3: *Chromatin density profiles for passive and motor cases without crosslinks and with chromatin–lamina linkage.* Chromatin density profiles, ϕ_c, as a function of radial distance R_s for passive, extensile, and contractile motor cases. (a) System without crosslinks or chromatin-lamina linkages ($N_c = 0$, $N_L = 0$). (b) System with chromatin-lamina linkages present but no crosslinks ($N_c = 0$, $N_L = 600$). All quantities are reported in simulation units (s. u.), where 1 s. u. of length = 1 μm and 1 s. u. of time = 0.5 s.

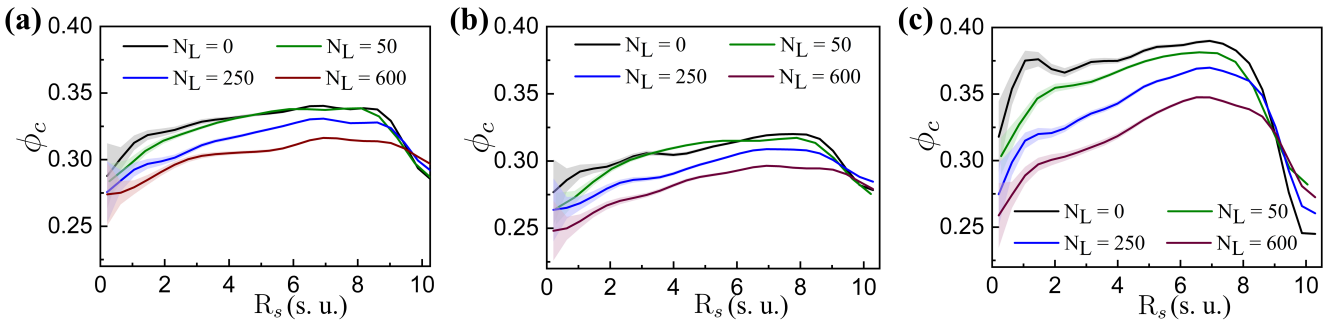


Fig. S4: *Chromatin distributions for passive, extensile, and contractile motors with varying chromatin–lamina linkages.* Chromatin density, ϕ_c, as a function of R_s for (a) passive, (b) extensile, and (c) contractile motors, shown for different chromatin-lamina linkage numbers (N_L) with a linear crosslink density profile. Results correspond to $N_c = 2000$ chromatin crosslinks. All quantities are reported in simulation units (s. u.), where 1 s. u. of length = 1 μm and 1 s. u. of time = 0.5 s.

Next, we investigate how chromatin distribution is influenced by varying the number of chromatin–lamina linkages while keeping the crosslink profile linear and the total number of chromatin crosslinks fixed at $N_c = 2000$. Figure S4 shows the resulting chromatin density profiles under passive, extensile, and contractile motor conditions. Both the passive and extensile cases yield nearly uniform radial density profiles, with extensile motor activity promoting chromatin decompaction relative to the passive and contractile cases (Fig. S4(a, b)). In contrast, contractile motors lead to significant chromatin compaction, resulting in a pronounced increase in density near the nuclear periphery. When no chromatin–lamina linkages are present, or when their number is low, the chromatin distribution remains relatively uniform, with slightly elevated density throughout the nucleus compared to cases with a higher number of linkages (Fig. S4c). However, increasing the number of linkages markedly enhances the spatial differentiation of chromatin density, with lower density in the nuclear interior and accumulation at the periphery (Fig. S4c).

2.3. Spatial distribution and dynamics of euchromatin and heterochromatin

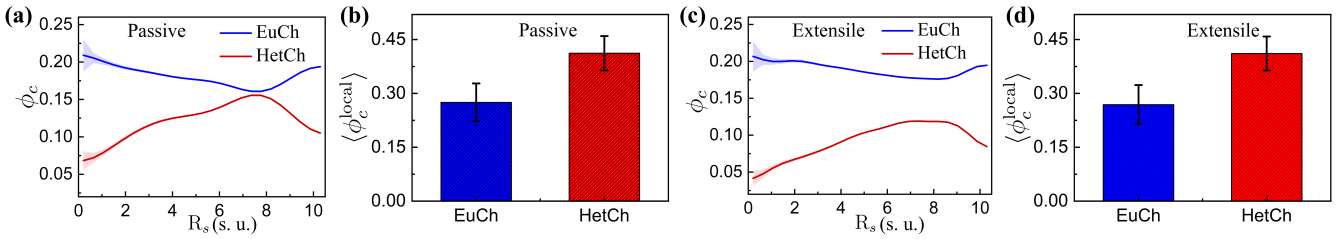


Fig. S5: *Euchromatin and heterochromatin density profiles for passive and extensile motor cases with a linear crosslink profile.* Density (ϕ_c) of euchromatin (EuCh) and heterochromatin (HetCh) as a function of R_s, along with the average chromatin density ($\langle\phi_c^{\rm local}\rangle$), for passive (a, b) and extensile motor (c, d) cases, for a linear crosslink density profile. The results correspond to $N_c = 2000$ chromatin crosslinks and $N_L = 600$ chromatin-lamina linkages. All quantities are reported in simulation units (s. u.), where 1 s. u. of length = 1 μm and 1 s. u. of time = 0.5 s.

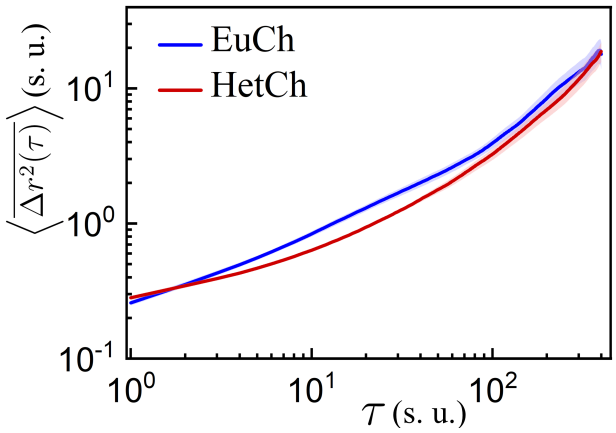


Fig. S6: *Dynamics of euchromatin and heterochromatin for contractile motors with a linear crosslink profile.* Mean square displacement $\left(\langle\overline{\Delta r^2(\tau)}\rangle\right)$ of euchromatin (EuCh) and heterochromatin (HetCh) for contractile motors with a linear crosslink density profile. The results correspond to $N_c = 2000$ chromatin crosslinks and $N_L = 600$ chromatin-lamina linkages. All quantities are reported in simulation units (s. u.), where 1 s. u. of length = 1 μm and 1 s. u. of time = 0.5 s.

2.4. Nuclear lamina shape fluctuations

To characterize shape fluctuations of the shell, a random slab passing through the center is selected, and the coordinates of the shell monomers within the slab are projected onto its plane. The spatial deviations of these monomers from the average shell radius are then analyzed using a fast Fourier transform (FFT), with F_q denoting the Fourier component of the deviation at wavenumber q. Fig. S7 presents the power spectrum of shape fluctuations for passive, extensile, and contractile motors with a linear crosslink profile, and for different crosslink density profiles corresponding to passive, extensile, and contractile motor cases. Contractile motors exhibit large-amplitude shape fluctuations, indicating more pronounced deformation of the nuclear lamina compared to extensile and passive cases (Fig. S7a). However, for a given motor case, qualitatively similar trends are observed across different crosslink density profiles (Fig. S7(b-d)).

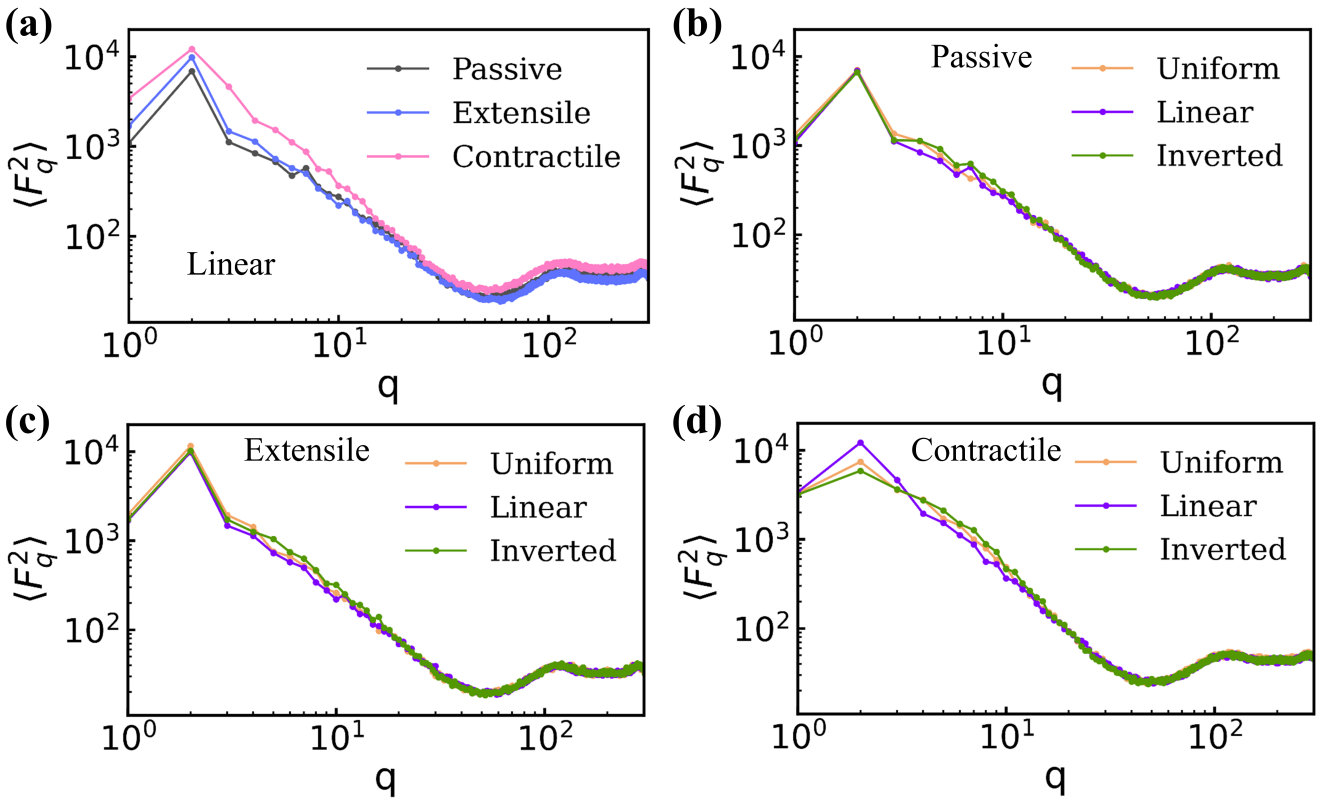


Fig. S7: *Nuclear shape fluctuations for different motor types and crosslink profiles.* Power spectrum of shell shape fluctuations for simulations with $N_c = 2000$ chromatin crosslinks and $N_L = 600$ chromatin-lamina linkages. (a) Different motor cases (passive, extensile, contractile) for a linear crosslink density profile. (b–d) Comparison of crosslink density profiles for (b) passive, (c) extensile, and (d) contractile motor cases.